Journal of Molecular Liquids 398 (2024) 124340

Contents lists available at ScienceDirect

Journal of Molecular Liquids

journal homepage: www.elsevier.com/locate/molliq

Aqueous Nitrogen-Nanobubble dispersion and supersaturation at elevated pressures up to 277 bara

Tesleem Lawal, Hao Wang, Ryosuke Okuno *

The University of Texas at Austin, Austin, Texas 78712, USA

ARTICLE INFO

Keywords:
Nanobubble
Supersaturation
Nitrogen
Solubility
Capillary pressure
Phase equilibrium

ABSTRACT

Aqueous nanobubble (NB) dispersion of gaseous species has been studied and applied for various processes near atmospheric pressure, but its fundamental properties are not well understood at elevated pressures. This paper presents an experimental program that measures the gas content of aqueous NB dispersion of nitrogen (N_2) at pressures up to 277 bara. The parameters directly set in the experiments were temperature, external pressure, and total volume while the overall composition of aqueous NB dispersion was obtained by constant mass expansion with material balance. The experimental data were analyzed by using a thermodynamic model for calculating an internally consistent set of properties at the experimental conditions.

Results show that the N_2 content in aqueous NB dispersion increased significantly with the system pressure. For example, the N_2 content at 277 bara was 0.29 mol/L for aqueous NB dispersion with deionized (DI) water, which was 2.3 times greater than the inherent solubility of N_2 in DI water at the same pressure. The effect of salinity was studied by using 0.88 M NaCl brine in place of DI water, but the N_2 contents were similar to those with DI water for the pressures tested in this research. Application of a thermodynamic model using the GERG-2008 equation of state to the experimental data indicates that NBs themselves were unlikely the main storage of N_2, but the existence of NBs enabled the supersaturation of the aqueous phase by N_2 because of capillary pressure.

1. Introduction

Aqueous nanobubble (NB) dispersion has been studied to increase the amount of the water-immiscible gaseous species (e.g., nitrogen, oxygen, and carbon dioxide) in an aqueous fluid beyond its inherent solubility. Two types of aqueous NB dispersions are surface nanobubbles and bulk nanobubbles. While the former refers to gas-filled cavities attached to surfaces in the form of spherical caps, the latter refers to gas-filled cavities freely suspended within a bulk liquid [1,2]. This paper is concerned with bulk NBs in the context of aqueous nanobubble dispersions.

NBs are classified as having diameters smaller than 1 μm. Studies have shown that their size depends on various parameters, such as gaseous species, pressure, pH, and other operating conditions of their generation [3–5]. The unique properties of NBs, such as enhanced gas concentration beyond the inherent solubility, kinetic stability, and enhanced interfacial area, have made them the subject of research in various fields [6–10]. Most industrial applications are for low-pressure open systems, such as agricultural applications [11], wastewater treatments [12–16], surface cleaning, and separation of materials [17–20]. Comprehensive reviews of NB generation techniques exist in the literature [3,10,21–24]. Commonly used techniques include cavitation (acoustic and hydrodynamic) [25–27], water electrolysis [28–30], compression-decompression [31–33], gas injection through porous (glass, ceramic, stainless steel) membranes [34–36], repeated compression of microbubbles [37,38], and mixing of gas and water [39].

The existence and long-term stability of NBs in low-pressure open systems have been discussed in the literature; for example, Alheshibri et al. [1] introduced the concept of Laplace Pressure Bubble Catastrophe (LBPC) regarding unstable nanobubbles. They suggested that, based on classical theories like the Young-Laplace equation and Epstein-Plesset theory [40], the significant pressure difference between the inside and outside of nanobubbles would cause them to dissolve rapidly in milliseconds or less. As the bubble radius decreases, the Laplace pressure increases exponentially, leading to accelerated dissolution.

Long-term stability of NBs has been observed even for low-pressure open systems for days [7,41,42], weeks [25,43,44], and months

* Corresponding author at: Center for Subsurface Energy and the Environment, The University of Texas at Austin, 200 E. Dean Keeton Street, Stop C0300, Austin, Texas 78712, USA.
E-mail address: okuno@utexas.edu (R. Okuno).

https://doi.org/10.1016/j.molliq.2024.124340
Received 10 October 2023; Received in revised form 21 February 2024; Accepted 23 February 2024
Available online 24 February 2024

Nomenclature

Abbreviations

CO_2	carbon dioxide
DFM	dark-field microscopy
DI	deionized
DLS	dynamic light scattering
EOR	enhanced oil recovery
EOS	equation of state
GCS	geological carbon sequestration
LPBC	Laplace Pressure Bubble Catastrophe
N_2	nitrogen
NaCl	sodium chloride
NB	nanobubble
N_C	number of components
NTA	nanoparticle tracking analysis
PDI	polydispersity index

Symbols

D	diffusion coefficient
d_h	hydrodynamic diameter
k_B	Boltzmann constant
m	mass
MW	molecular weight
P	pressure
T	temperature
V	volume
x	gas content
Z	compressibility factor
ρ	density
η	dynamic viscosity

Subscripts

b	brine
cell	sapphire cell
w	water

Table 1
Experiment variables for the gas content measurement.

Variable	Variations	Other conditions
Salinity	DI water, NaCl brine	35–277 bara; 5 μm
Co-injection ratio	50 % N_2; 50 % DI water (or NaCl brine)	35–277 bara; 5 μm
	60 % N_2; 40 % DI water	70, 139, 208 bara; 5 μm
Total injection flow rate	100 mL/h	35–277 bara; 5 μm
	500 mL/h	70, 139, 208 bara; 5 μm
Membrane pore diameter	2 μm	70, 139, 208 bara

[26,36,45]. Light scattering techniques (e.g., dynamic light scattering or DLS and nanoparticle tracking analysis or NTA) [20,26,32,36,37,41], resonant mass measurements [46,47], high-resolution imaging techniques (e.g., transmission electron microscopy and scanning electron microscopy) [5,48,49], and spectral techniques have been used to verify the existence of NBs [25,39]. These techniques, however, have been limited in differentiating between nanobubbles and nanoparticles. They are also not easily adapted to measurements of high-pressure aqueous NB samples because of the requirement of specially designed experiment rigs.

Most discussions on NB stability were made for open systems near atmospheric pressure, and many did not even specify the system for their analysis. Unlike those studied in the literature, the current paper is focused on a high-pressure closed system of aqueous NB dispersion. As will be shown in this paper, the enhanced gas content by aqueous NB dispersion tends to be more significant at a higher pressure (therefore, a closed system); hence, this research was motivated by potential applications of aqueous NB dispersion for subsurface processes, such as enhanced oil recovery (EOR) and geological carbon sequestration (GCS). For example, carbonated water injection has been studied for EOR [50–62] and also has attracted attention for CO_2 in-situ mineralization as GCS since the CarbFix project in Iceland [63–67]. An obvious limitation of carbonated water is the CO_2 concentration limited by the inherent solubility (e.g., 1 mol/L).

Although aqueous NB dispersion has the potential to enhance the gas content in aqueous fluid as widely studied for open systems near atmospheric pressure, its fundamental properties are not well understood especially at elevated pressures relevant to subsurface applications. This is at least in part because it is not easy to directly measure properties of aqueous NB dispersion under elevated pressure, such as gas content, bubble size, bubble number density, phase composition, capillary pressure, and interfacial tension, which are expected to vary for different pressure, temperature, gas species, salinity, and operation conditions of NB generation. Hence, there is a critical need to generate fundamental experimental data on aqueous NB dispersion at elevated pressures. To this end, we started by using nitrogen (N_2), instead of CO_2, as the gaseous species in this research since CO_2 dissolution in water gives additional complexities associated with a pH change.

This paper presents an experimental program that measures the gas content of aqueous N_2 NB dispersion at pressures up to 277 bara and analyzes the data using a thermodynamic model. The parameters directly set in the experiments were temperature, external pressure, and total volume, while the overall composition of aqueous NB dispersion was obtained by constant mass expansion. The limited amount of data that were directly measured was supplemented by a thermodynamic model, which generated a consistent set of properties, including those not directly measurable, such as bubble size, number density, and capillary pressure. The depressurized samples were subjected to measurement of bubble size distribution and bubble number density using DLS and NTA.

To the best of our knowledge, this is the first experimental study of NB generation and gas content measurement at high pressures, addressing a critical research gap in the literature. Furthermore, the enhancement of gas content in water in the form of nanobubble dispersions holds immense potential for accelerating storage security in GCS applications and enhancing oil recovery.

2. Experimental methods

2.1. Materials

The aqueous samples used in the experiment were deionized (DI) water and sodium chloride (NaCl) brine with a salinity of 50,000 ppm (equivalent to 0.88 M NaCl). The DI water had a resistivity of 18.2 MΩ-cm. NaCl salt (Thermo Scientific Chemicals, purity of 99.0 %) was dissolved in DI water to formulate the brine solution. The aqueous solutions were checked for impurities using a NanoSight NS500 instrument and no particles (impurities) were confirmed. Nitrogen gas of research-grade (Linde Gas & Equipment, purity of 99.9999 %) was used.

2.2. Gas content measurement

The N_2 gas content measurement was performed in two stages. The first stage was the generation and preparation of the NB sample while

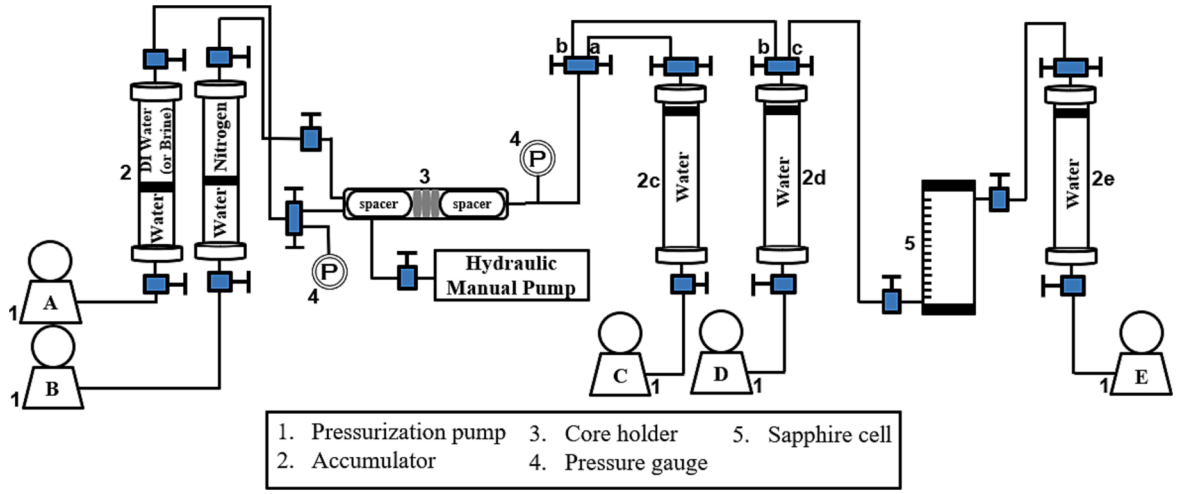

Fig. 1. Schematic of the experimental setup used to generate the aqueous N_2 NB fluid.

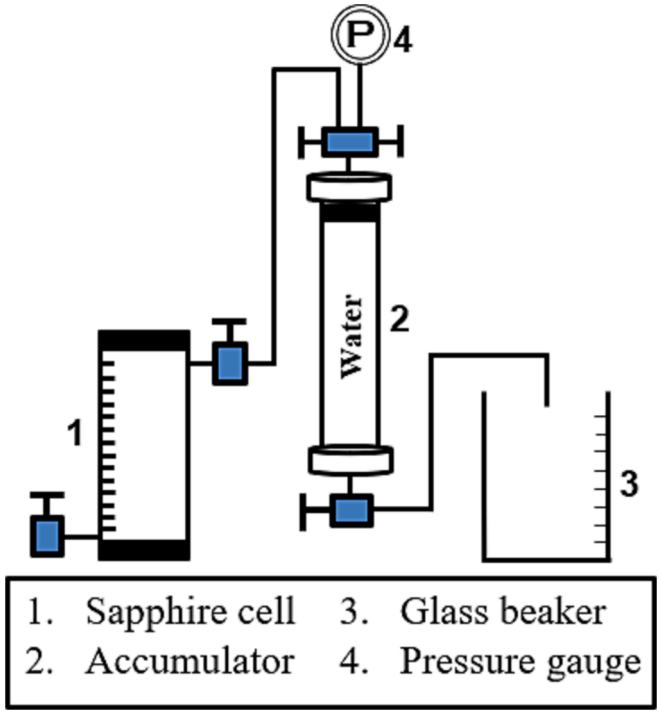

Fig. 2. Schematic of the experimental setup to measure the gas content in the aqueous N_2 NB fluid.

the second stage was the depressurization and measurement of the N_2 gas content. Several variables—pressure, salinity, volumetric co-injection ratio, total injection flow rate, and membrane pore diameter—were tested for the gas content measurements. Table 1 shows the variables investigated for the gas content measurements. All the experiments were conducted at room temperature (295.15 K). The control experiments used DI water, a co-injection ratio of 50 % N_2 + 50 % DI water, a total injection flow rate of 100 mL/h, a membrane pore diameter of 5 μm, and pressures ranging from 35 to 277 bara.

Stage 1: Generation and preparation of NB sample.

Fig. 1 shows a schematic of the experimental setup for generating the N_2 NB. The setup consists of five accumulators: two accumulators for N_2 and DI water (or NaCl brine) and three receiver accumulators; three stainless-steel porous membranes; one Hassler-type core holder with a 70 Durometer Viton sleeve to house the membranes; spacers on either side of the membranes; a hydraulic manual pump to maintain confining pressure on the core holder; pressure gauges to monitor experiment pressures; Teledyne ISCO syringe pumps to control pressure and flow rates; and a sapphire visualization cell.

The stainless-steel porous membrane had a porosity of 37 %, an average pore size of 5 μm (with a maximum size of 10 μm), an outer diameter of 25.4 mm, and a length of 3 mm. The spacers on either side of the membranes had fluid dispersion channels engraved on the cross-sectional surface to allow for full distribution of fluid across the entire face of the membranes. A confining pressure of 35 bara greater than the experiment pressure was applied to the core holder for each experiment. The pressure gauges were zeroed before each experiment to ensure accurate and consistent pressure readings across all experiments. The sapphire cell was used to visually monitor the behavior of the NB sample and has a known volume (including all connection lines), V_{cell}, of 13.69 mL. It can withstand pressures up to 350 bara and temperatures up to 423.15 K. To prevent gas trapping in any of its connections, the sapphire cell was configured to simulate a single-inlet single-outlet cell by connecting valves to all its connection ports. Upon completion of each experiment, the entire system was thoroughly cleaned with DI water and dried with air before proceeding to the next experiment.

Before generating the NB, the entire system was evacuated for 1 h. The system was saturated with DI water (or NaCl brine) up to receiver accumulator #1 (2c in Fig. 1) at the experiment pressure. The sapphire cell and the top of receiver accumulators #2 and #3 (2d and 2e in Fig. 1) were filled with N_2 at the experiment pressure. To generate the NB, N_2 and DI water (or NaCl brine) were co-injected (per the different configurations shown in Table 1) at a constant flow rate through the porous membranes at the specified pressure, co-injection ratio, and total injection flow rate. The co-injected fluids were received downstream of the porous membranes at a constant refill flow rate (maintaining the system pressure) into receiver accumulator #1 until a steady state was reached. After reaching a steady state (approximately 3 min for 500 mL/h and 15 min for 100 mL/h), the co-injected fluids were then received by receiver accumulator #2 at a constant refill flow rate. The duration of the co-injection was 60 min for 100 mL/h and 12 min for 500 mL/h. We posit that the formation of nanobubbles occurs in two main stages: first, hydrodynamic mixing and gas snap-off across the membrane leads to the creation of dispersed N_2 bubbles in the aqueous phase that is supersaturated by N_2, and secondly, the bulk microbubbles are compressed to form bulk nanobubbles under elevated pressure conditions.

After the co-injection period, receiver accumulator #2 contained excess bulk N_2 as well as the N_2 NB. The contents of receiver #2 were then injected through the sapphire cell into receiver #3 at a constant flow rate. First, the N_2 gas initially in the sapphire cell was displaced by

Table 2
Measured gas content data for aqueous N_2 NB in DI water at 295.15 K.

P_1 (bara)	P_2 (bara)	m_{w2} (g)	m_{w3} (g)	V_{cell} (mL)	x_{N2} (mol/L)	Inherent solubility (mol/L)	Solubility enhancement
34.59	1.22	4.54	10.765 ± 3	13.69	0.0515	0.0160	3.22
68.93	1.29	11.4	10.930 ± 3	13.69	0.0801	0.0310	2.58
104.2	1.15	23.58	11.405 ± 3	13.69	0.1118	0.0575	1.94
103.3	1.29	19.49	11.310 ± 3	13.69	0.1098	0.0574	1.91
103.4	1.29	21.22	11.295 ± 3	13.69	0.1165	0.0574	2.03
138.2	1.22	32.01	11.040 ± 3	13.69	0.1505	0.0726	2.07
207.8	1.22	57.41	11.834 ± 3	13.69	0.2401	0.1026	2.34
277.1	1.22	71.92	12.040 ± 3	13.69	0.2922	0.1270	2.30

the excess bulk N_2 from receiver #2. Then, the bulk N_2 was further displaced by the N_2 NB. We ensured the cell contained only N_2 NB with no trapped gas by injecting at least twice the cell volume of N_2 NB into the cell. After filling the cell with the N_2 NB, the top and bottom valves of the cell were closed to isolate the cell from the other parts of the system. The sapphire cell then contained the aqueous NB fluid sample at pressure, P_1.

Stage 2: Depressurization and gas content measurement.

Fig. 2 shows a schematic of the experimental setup for measuring the gas content in the generated N_2 NB. The setup consists of a sapphire cell containing the NB sample, a piston accumulator with a pressure gauge, and a glass beaker.

The sapphire cell was connected to the accumulator via a stainless-steel tubing. The piston of the accumulator was set at the top of the accumulator. The dead volumes of the tubing and the accumulator were known. Before depressurizing the N_2 NB sample, the tubing and dead volume of the accumulator were evacuated for 15 min. Then, the N_2 NB sample was gradually depressurized. First, the top valve of the sapphire cell was slowly opened to fill the tubing with depressurized N_2 escaping the NB sample. Then, the top valve of the accumulator was slowly opened to allow further escape of N_2 from the NB sample into the accumulator. Finally, the bottom valve of the accumulator was opened to collect water to gauge the displacement of the piston as the aqueous NB fluid sample was depressurized or expanded. The water collected corresponded to the volume of depressurized N_2 in the aqueous NB fluid. The mass of the water collected is denoted as m_{w2}, and the pressure at the top side of the accumulator after depressurization is P_2. Finally, the remaining water (or brine) in the cell was collected and its mass m_{w3} was measured. The atmospheric pressure, P_3, during the experiment was 1.0135 bara.

The N_2 gas content was calculated on the following basis:

1. There was a negligible amount of N_2 in the remaining water phase in the sapphire cell because the solubility of N_2 in water at atmospheric pressure is small and because the presence of any bubbles has a negligible impact on the gas content as shown later for NTA data.
2. The amount of water, mw_3, was corrected for the transfer of water to the expanded gas phase as mist.

The gas content, represented in units of mole per liter (mole of N_2 in a volume of aqueous NB fluid), was then calculated as shown below:

$$x_{N_2}(mol/L) = \frac{\text{mole of } N_2 \text{ (mol)}}{\text{volume of NB sample (L)}} \quad (1)$$

$$\text{mole of } N_2(\text{mol}) = \frac{\rho_1 V_1}{MW_{N_2}} = \left(\frac{\rho_1}{MW_{N_2}}\right)\left(\frac{P_2 V_2 Z_1}{P_1 Z_2}\right) \quad (2)$$

where ρ_1 is the density of N_2 at the experimental pressure, V_1 is the volume of N_2 in the aqueous NB fluid at experimental pressure, MW is the molecular weight of N_2, P_1 is the experimental pressure, P_2 is the depressurized pressure, V_2 is the total volume of N_2 at atmospheric pressure, Z_1 is the compressibility factor of N_2 at the experimental pressure, and Z_2 is the compressibility factor of N_2 at atmospheric pressure.

The gas content data was compared to the thermodynamic solubility of N_2 in water at 298.15 K [68] and N_2 in NaCl brine at 295.15 K [69] to determine the solubility enhancement factor of aqueous NB fluids. For each configuration shown in Table 1, the procedure remained the same. The repeatability of the experiment was tested by repeating the experiments three times at 104 bara for DI water. The standard deviation from these experiments was applied to the remaining experiments as error bars.

2.3. Bubble size measurement for depressurized samples

The size distribution, number density, mean, and mode of the N_2 NB were measured for depressurized samples at atmospheric pressure using two light scattering techniques: dynamic light scattering (DLS) and nanoparticle tracking analysis (NTA). The samples for the bubble size measurement were generated using the same procedure described in Section 2.2. Upon isolating the sapphire cell, however, the sample in the cell was depressurized to atmospheric pressure similarly to the method of compression-decompression [31–33] for low-pressure bulk nanobubble generation. The depressurized sample containing N_2 NBs at atmospheric pressure was transferred into glass vials and stored at room temperature. Bubble size measurements were performed 1, 2, 7, and 10 days after the NB formation. On day 1, the measurements were performed 1 h after depressurization, and on the subsequent days, the measurements were performed 26, 147, and 217 h after depressurization. Before measuring the size distribution of the samples, DLS and NTA measurements of the DI water sample were performed three times, and no particles were detected.

The DLS measurements used a ZEN3500 Zetasizer Nano ZS particle size analyzer (Malvern Panalytical Ltd.). DLS is a non-invasive scattering technique that measures particle sizes by capturing the random change in intensity of light scattered by particles undergoing Brownian motion within an aqueous medium. The fluctuations in scattered light intensity are then translated into particle sizes using the Stokes-Einstein equation:

$$d_h = \frac{k_B T}{3\pi\eta D} \quad (3)$$

where d_h is the hydrodynamic diameter, k_B is the Boltzmann constant, T is the temperature, η is the dynamic viscosity of the aqueous phase, and D is the diffusion coefficient of particles in the aqueous phase.

The Zetasizer Nano ZS can determine a particle size distribution within the range from 4 nm to 3 μm. The experiments were performed at 295.15 K to maintain consistent conditions and with a refractive index of 1.33 for water and 1.0 for N_2. The particle intensity distribution is determined directly from the measurements and is then mathematically transformed into a number distribution. The measurements were taken at a fixed scattering angle of 173 degrees and repeated twice for each sample.

The NTA measurements used a NanoSight NS500 (Malvern Panalytical Ltd.). The NTA technique, built upon dark-field microscopy (DFM), tracks individual particle trajectories to compute sizes based on the Stokes-Einstein equation. The measurements were performed at

Table 3
Measured gas content data for aqueous N_2 NB in 50,000 ppm NaCl brine at 295.15 K.

P_1 (bara)	P_2 (bara)	m_{w2} (g)	m_{b3} (g)	V_{cell} (mL)	x_{N2} (mol/L)	Inherent solubility (mol/L)	Solubility enhancement
47.07	1.22	3.53	11.155 ± 3	13.69	0.0463	0.0239	1.94
69.82	1.22	9.01	11.850 ± 3	13.69	0.0637	0.0342	1.86
103.0	1.22	19.98	10.800 ± 3	13.69	0.1075	0.0481	2.23
138.5	1.29	27.62	11.530 ± 3	13.69	0.1402	0.0617	2.27
207.8	1.29	43.66	11.800 ± 3	13.69	0.2008	0.0854	2.35
274.0	1.36	66.55	11.980 ± 3	13.69	0.3037	0.1051	2.89

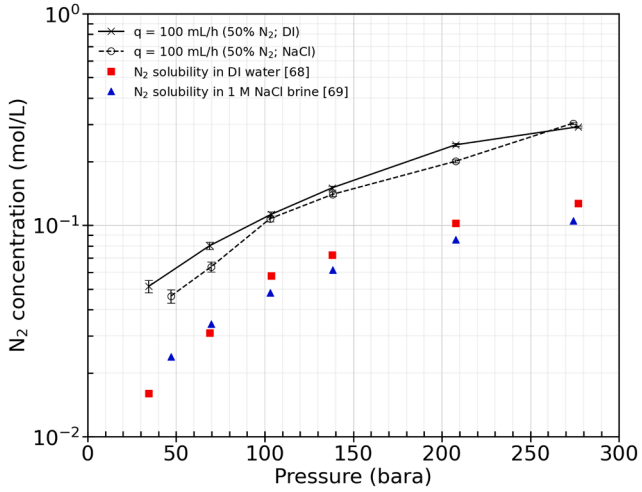

Fig. 3. N_2 gas content in DI water and 50,000 ppm NaCl brine. The red squares represent the thermodynamic solubility of N_2 in water [68]. The blue triangles represent the thermodynamic solubility of N_2 in NaCl brine [69]. (For interpretation of the references to colour in this figure legend, the reader is referred to the web version of this article.)

room temperature and the settings for screen gain, focus, camera level, and detection threshold were optimized to ensure accurate detection of particles while minimizing noise. Each sample was recorded three times and the duration of each capture was 30 s. One advantage of NTA over DLS is its capability to determine the number density of particles in an aqueous medium.

The DLS and NTA measurements in this research were only for depressurized samples of aqueous NB dispersion, and their application to high-pressure samples is currently not available. Although the measurement conditions are different from the envisioned applications to high-pressure processes, the DLS and NTA data are useful to validate the samples of aqueous NB dispersion and to observe the transient behavior of depressurized samples in an open system. Also, low-pressure data serve as a reference for high-pressure data with a correlative capability of a thermodynamic model in this research.

3. Results and discussion

3.1. Effect of pressure and salinity

Tables 2 and 3 show the measured gas content data in the experiments for aqueous N_2 NB fluid in DI water and 50,000 ppm NaCl brine, respectively. Fig. 3 presents the gas content data in mol/L for DI water and NaCl brine at a constant co-injection ratio of 50 % N_2 + 50 % DI water (or NaCl brine), a total injection flow rate of 100 mL/h, and a 5 μm membrane. The red squares and blue triangles in Fig. 3 represent the inherent solubility of N_2 in water and NaCl brine, respectively. The error bars in Fig. 3 represent an estimate of the variability in the experimental measurements. Note that x_{N2} in Tables 2 and 3 and Fig. 3 represents the overall N_2 concentration including the dispersion of N_2 bubbles and the dispersion of N_2 molecules in the external aqueous phase.

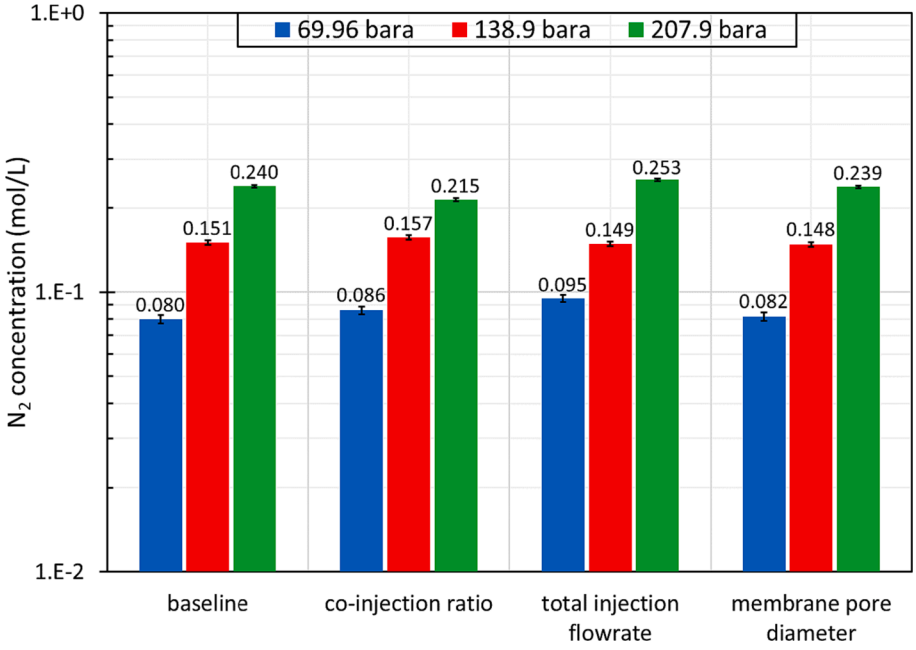

Fig. 4. N_2 gas content in DI water at different operating conditions (co-injection ratio, total injection flow rate, and membrane pore diameter) and different pressures. The baseline case used a co-injection rate of 50 % N_2 + 50 % DI water through a 5 μm membrane at a total injection flow rate of 100 mL/h.

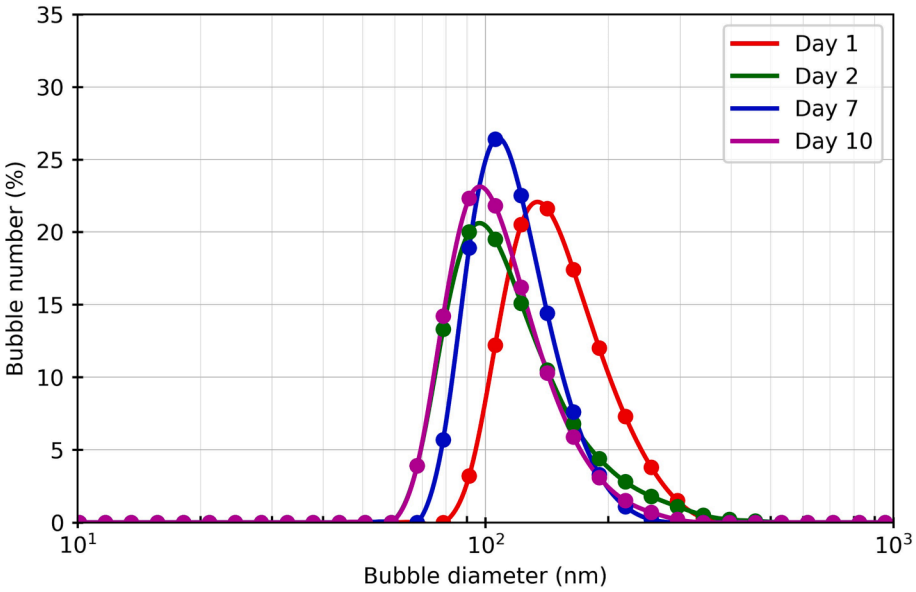

Fig. 5. Size distribution of the aqueous N_2 NB sample using DLS.

Table 4
Mean, mode, PDI, and diffusion coefficients of the aqueous N_2 NB sample using DLS.

Day	Bubble size, mean (nm)	Bubble size, mode (nm)	PDI	Diffusion coefficient (m^2/s)
1	235.1 ± 7.43	158.6 ± 5.45	0.354 ± 0.05	(1.93 ± 0.06) × 10^{-12}
2	169.6 ± 5.09	132.4 ± 14.9	0.112 ± 0.16	(2.67 ± 0.08) × 10^{-12}
7	212.3 ± 6.08	134.0 ± 20.9	0.359 ± 0.01	(2.13 ± 0.06) × 10^{-12}
10	156.7 ± 10.9	107.7 ± 7.28	0.243 ± 0.26	(2.90 ± 0.20) × 10^{-12}

The results show that as pressure increased from 35 to 277 bara, the gas content increased significantly for both DI water and NaCl brine. Note that this figure shows the N_2 concentration on a logarithmic scale. The gas content in aqueous NB dispersion with NaCl brine was close to that with DI water across all the pressures tested. Thus, the 0.88 M NaCl brine had no significant impact on the N_2 gas content in the aqueous NB sample. The N_2 concentration in the N_2 NB dispersion with NaCl brine was 1.9 times greater than the inherent solubility at 69.8 bara, and the enhancement factor was as large as 2.9 at 274.0 bara as shown in Table 3. An extrapolation of the gas content data to atmospheric pressure for DI water gives an N_2 gas content of 0.0121 mol/L (or 4.7 × 10^{-4} mol fraction of N_2).

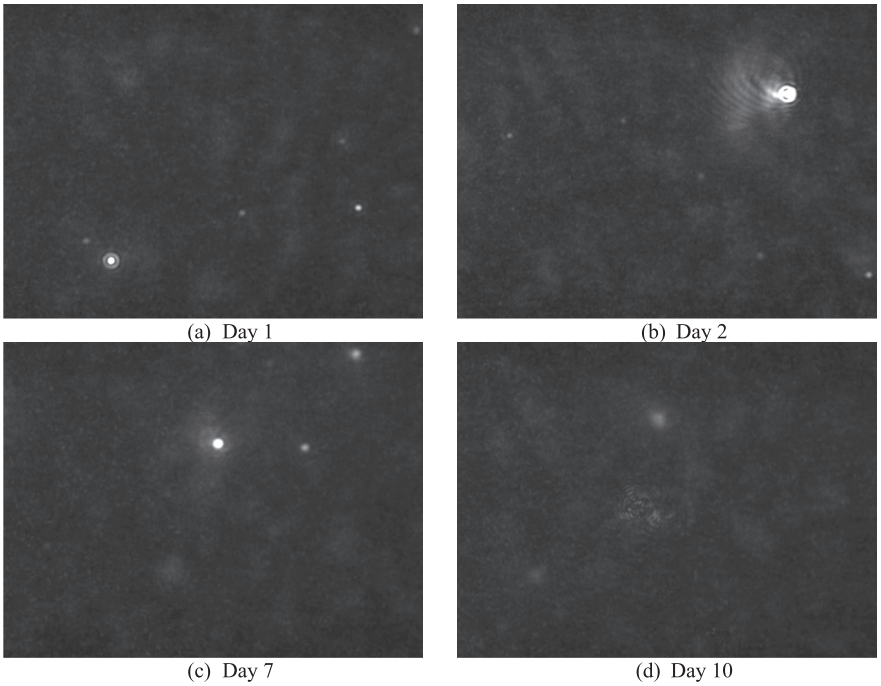

Fig. 6. Laser-illuminated N_2 NB in DI water using NTA.

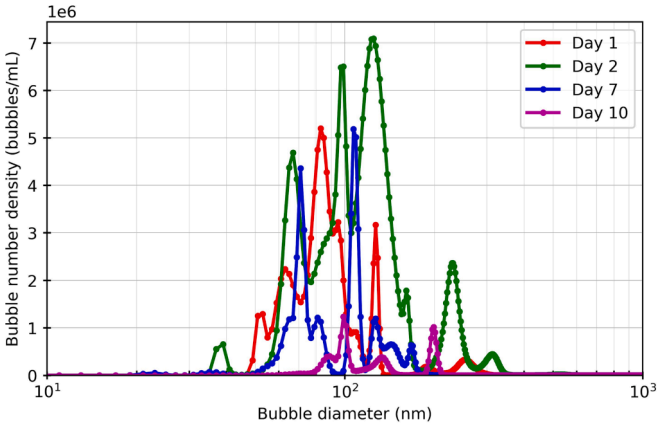

Fig. 7. Size distribution of the aqueous N_2 NB sample using NTA.

Table 5
Mean, mode, bubble number density, and diffusion coefficients of the aqueous N_2 NB sample using NTA.

Day	Bubble size, mean (nm)	Bubble size, mode (nm)	Bubble number density (bubbles/mL)	Diffusion coefficient (m^2/s)
1	101.8 ± 11.9	97.90 ± 14.6	$(9.25 \pm 0.63) \times 10^7$	$(4.74 \pm 0.92) \times 10^{-12}$
2	116.5 ± 20.4	103.2 ± 11.0	$(2.56 \pm 1.39) \times 10^8$	$(4.20 \pm 1.12) \times 10^{-12}$
7	103.2 ± 6.30	84.70 ± 12.5	$(5.85 \pm 2.18) \times 10^7$	$(4.45 \pm 0.47) \times 10^{-12}$
10	128.0 ± 17.8	102.1 ± 8.60	$(1.72 \pm 0.69) \times 10^7$	$(3.67 \pm 0.78) \times 10^{-12}$

3.2. Effect of coinjection ratio, total injection rate, and membrane pore diameter

Fig. 4 shows the effects of co-injection ratio, total injection flow rate, and membrane pore diameter at different pressures on the gas content of N_2 in the aqueous NB sample (DI water). Overall, the results show negligible impacts of co-injection ratio, total injection flow rate, and membrane pore diameter on the N_2 gas content compared to the baseline experiments. These results are in contradiction to the results reported for low-pressure experiments [4,35,45] about the effect of changing the co-injection ratios or pore membrane diameters on gas content data. This is likely because these effects were significant and noticeable at low pressures and then became less significant at high pressures; that is, increasing the pressure had the most significant impact on the N_2 gas content in DI water and NaCl brine among the experimental parameters tested in this research.

3.3. Bubble size measurement using DLS and NTA

Fig. 5 shows the size distributions of depressurized samples for aqueous NB dispersion of N_2 in DI water based on DLS. Table 4 shows the mean and mode bubble sizes, polydispersity indices (PDI), and diffusion coefficients from the DLS measurements on days 1, 2, 7, and 10. Before the measurements, the DI water used to generate the NB was checked for the presence of nanosized impurities and none were detected.

The DLS data show notable trends in bubble size over time. On day 1, the mean bubble size was 235.1 nm, which decreased to 169.6 nm on day 2, followed by an increase to 212.3 nm on day 7, and a subsequent decrease to 156.7 nm on day 10. The mode of the bubble size was 158.6, 132.4, 134.0, and 107.7 nm for days 1, 2, 7, and 10, respectively. The difference in behavior between the mean and mode bubble sizes comes from the transient distribution of bubble sizes as given in Fig. 5. The PDI data also reflect the transient size distribution using DLS. On day 1, the PDI was 0.354, correlating to a mean size significantly larger than the mode size. This suggests the presence of a substantial number of larger bubbles contributing to the scattered light signal. However, on day 2, the PDI dropped to 0.112, indicating the absence of significantly larger bubbles. On day 7, the PDI increased to 0.359, possibly indicating the coalescence of smaller bubbles into larger bubbles, causing the mean size to become greater than the mode size. Finally, on day 10, the PDI decreased again to 0.243, further confirming the reduction in the number of larger particles, and thus a reduction in the mean bubble size. The PDI behavior gives credence to the presence of gas-filled nanobubbles which tend to coalesce into larger bubbles and eventually dissipate either through bursting or rising to the surface.

Fig. 6 shows the laser-illuminated N_2 nanobubbles using NTA at atmospheric pressure on days 1, 2, 7, and 10. The detected nanobubbles are shown as white dots on a black background. One advantage of NTA over DLS is its capability to determine a bubble number density in the

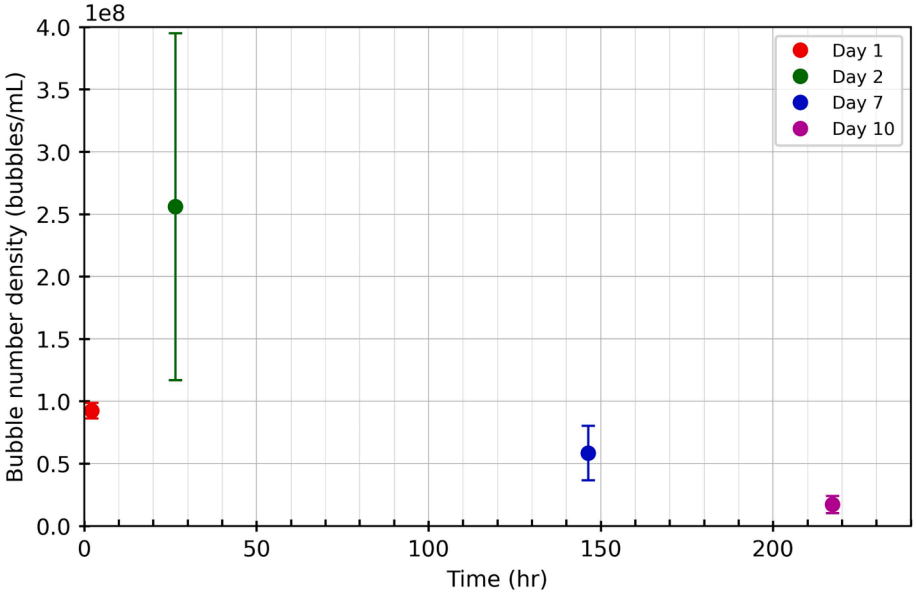

Fig. 8. NB number density of the aqueous N_2 NB samples using NTA.

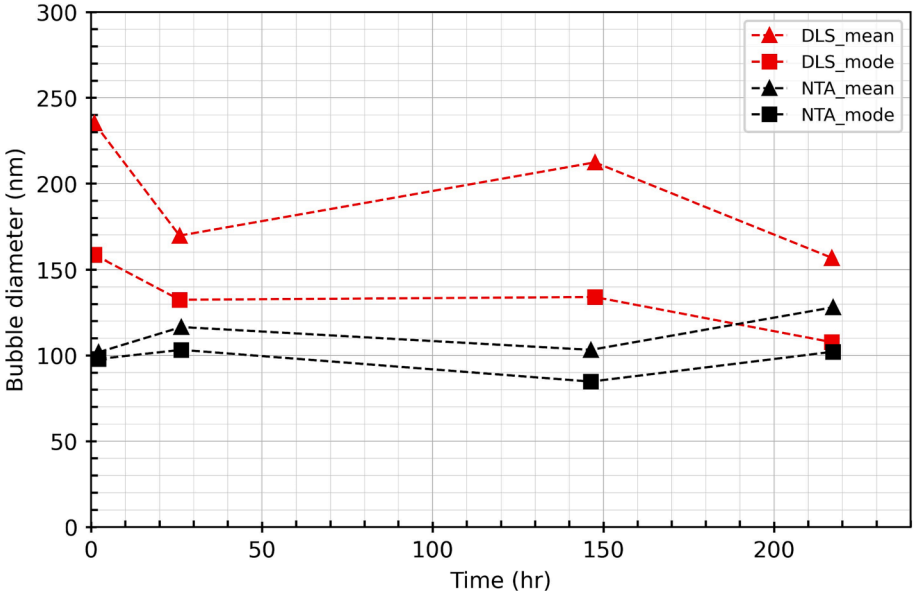

Fig. 9. Mean and mode of the aqueous N_2 NB sample using DLS and NTA.

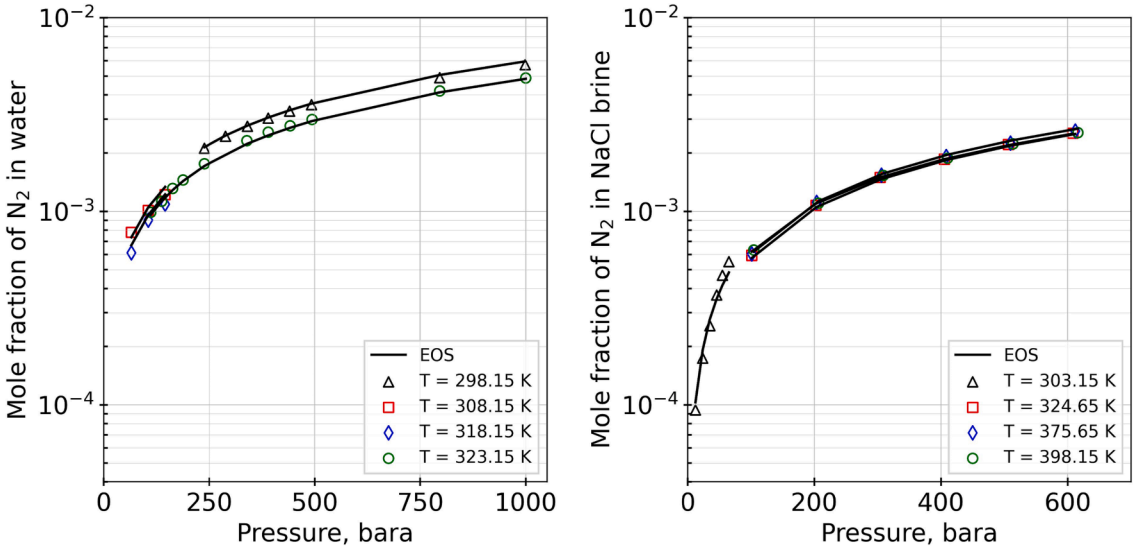

Fig. 10. Calibrated GERG-2008 EOS model for the N_2/water [78,79] and N_2/NaCl brine [70,71] solubility data at different pressures and temperatures.

sample. Fig. 7 shows the size distribution of the N_2 NB in DI water. Table 5 gives the mean and mode bubble sizes, bubble number densities, and diffusion coefficients from the NTA measurements. The transient behavior of NB size distribution is also shown in Fig. 8. Like the DLS measurements, the DI water used to generate the NB for the NTA measurements was checked for the presence of nanosized impurities and no impurities were detected.

Figs. 7 and 8 show that the overall behavior of aqueous NB dispersion became more stabilized over time, suggesting that the numerical results given in Tables 4 and 5 should be carefully understood together with the overall trends shown in Figs. 5, 7, and 8.

On day 1, the mean bubble size was 101.8 nm, and the mode bubble size was 97.9 nm with a bubble concentration of 9.25×10^7 bubbles/mL. There was a close agreement between the mean and mode bubble sizes. On day 2, both the mean and mode bubble sizes increased to 116.5 nm and 103.2 nm, respectively, with a notably higher number density of 2.56×10^8 bubbles/mL. The results from days 1 and 2 show a significant level of transient behavior of aqueous NB dispersion with the possibilities of bubble coalescence, growth, and nucleation over time. On day 7, the mean bubble size slightly decreased to 103.2 nm, and the mode bubble size decreased to 84.7 nm. The number density was 5.85×10^7 bubbles/mL. Finally, on day 10, the mean bubble size increased to 128.0 nm, while the mode bubble size also increased to 102.1 nm with a number density of 1.72×10^7 bubbles/mL.

Fig. 9 compares DLS and NTA measurements at atmospheric pressure in terms of mean and mode bubble sizes. NTA measurements show a closer agreement between the mean and mode sizes than DLS measurements. This is because of the inherent difference in the measurement principles of both measurement techniques. That is, NTA measures the rate of Brownian motion of the bubbles while DLS measures the fluctuations in the scattered light intensity of the bubbles undergoing Brownian motion. This fundamental difference leads to NTA being less susceptible to polydispersity, thus, showing a closer agreement between the mean and mode bubble sizes.

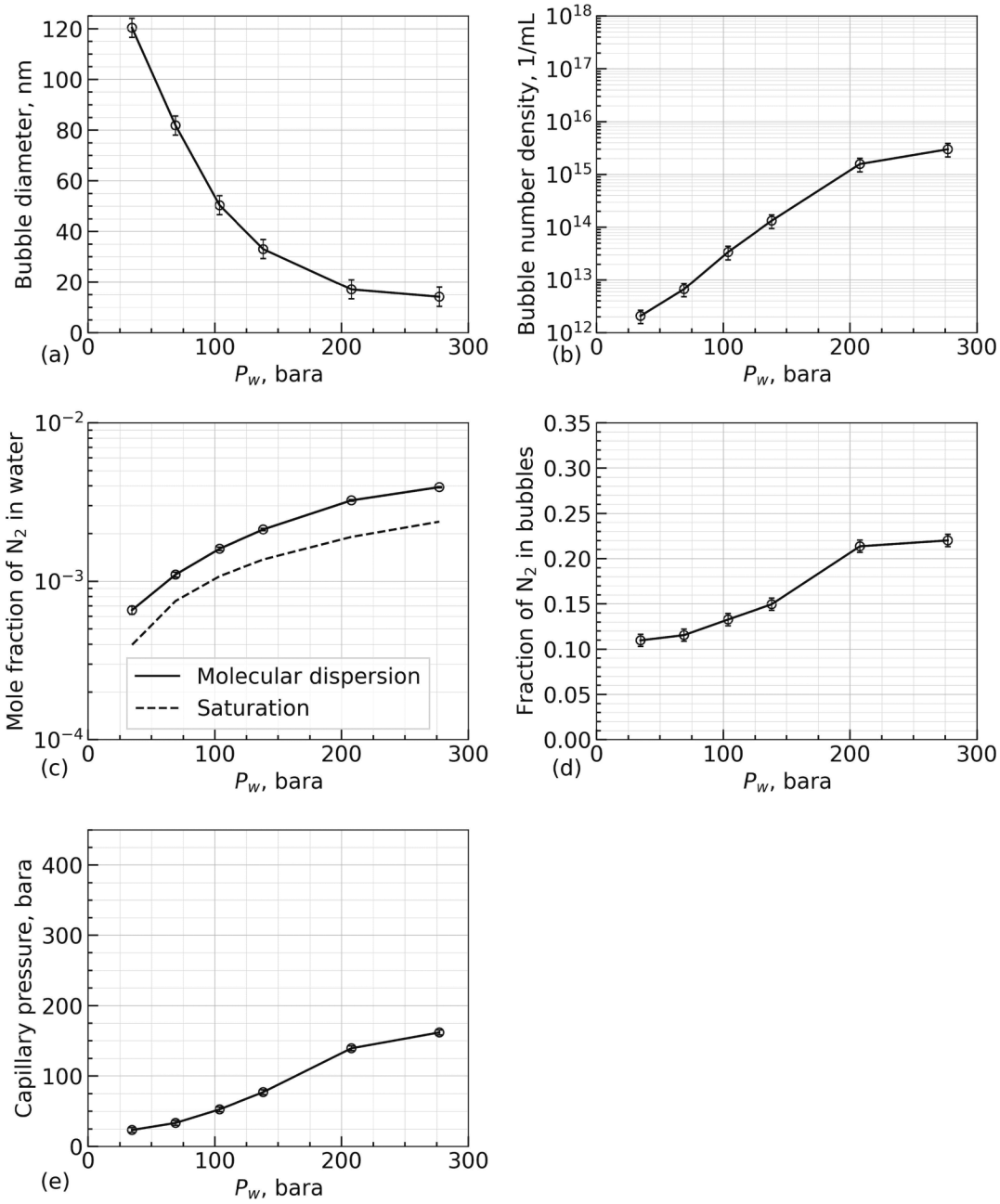

Fig. 11. Bubble diameter, bubble number density, N_2 mole fraction, fraction of N_2 contained in bubbles, and capillary pressure of aqueous NB fluid in DI water at 295.15 K for pressures up to 277 bara.

3.4. Thermodynamic analysis of aqueous NB dispersion of N_2

The most important benefit of using thermodynamics to analyze the experimental data in this research is that a thermodynamic model can give an internally consistent set of properties for the entire experimental conditions, which enables understanding the overall behavior of aqueous NB dispersion. Also, such properties include unmeasurable ones in high-pressure experiments, such as phase composition and capillary pressure. As described previously, the experimental procedure directly specifies the temperature, total volume, and pressure of a closed system of aqueous nanobubble dispersion of N_2. Then, the constant mass expansion of the system gives the mole numbers of water and N_2. With these experimentally measurable variables, the most convenient approach to analyzing the experimental data is to minimize the Helmholtz free energy using a thermodynamic model [73]. Then, a solution for the minimization problem gives thermodynamic properties for the dispersion of N_2-rich nanobubbles in the aqueous phase that is supersaturated by N_2 at the experimental conditions.

The traditional two-phase system with a planar interface requires $N_C + 2$ variables to be set, where N_C is the number of components; however, the current problem requires setting $N_C + 3$ variables. The additional variable comes from the generalization to allow for different pressures for the two phases (i.e., capillary pressure). In this research, the $N_C + 3$ variables are temperature, total volume, aqueous-phase pressure, and mole numbers of the components (water and N_2). With these specifications, this section describes properties of the aqueous NB dispersions generated in the experiments using a single thermodynamic model, which gives internal consistency of the calculated properties. We recognize limitations of the modeling; for example, the binary system (water and N_2) requires a uniform size of bubbles, and the mole numbers

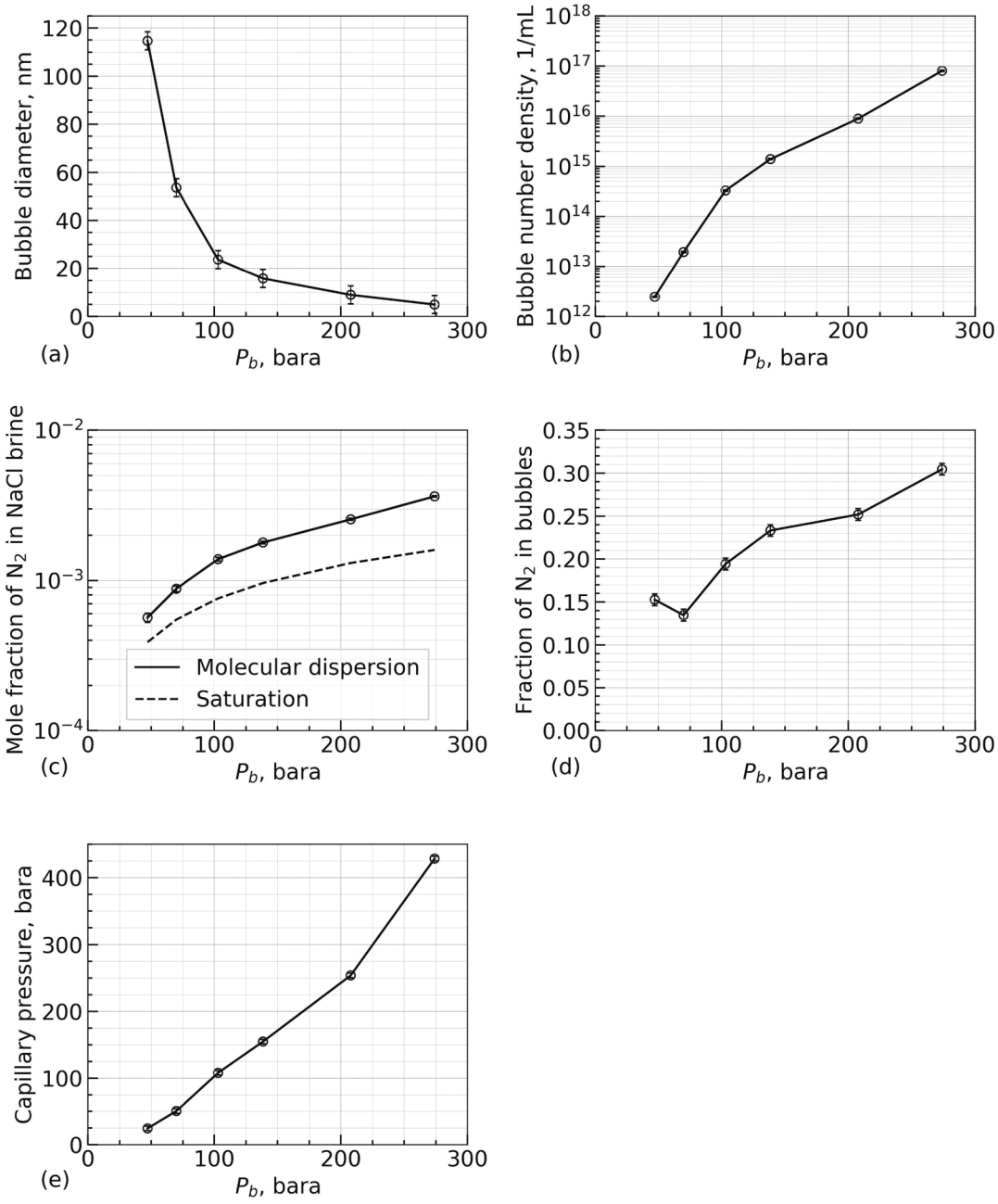

Fig. 12. Bubble diameter, bubble number density, N_2 mole fraction, fraction of N_2 contained in bubbles, and capillary pressure of aqueous NB fluid in NaCl brine at 295.15 K for pressures up to 274 bara.

of water and N_2 (from the constant mass expansion) contain uncertainty. Therefore, thermodynamic properties given for aqueous NB dispersions in this section must be understood as apparent values satisfying experimentally specified conditions and material balance.

The modeling approach largely follows Achour and Okuno [73] and Achour et al. [74], but we have extended it to cover all experimental conditions in this research. The GERG-2008 equation of state (EOS, [75]) was used because the EOS used in this research should be reliable in constructing the Helmholtz free energy surface in metastable regions [76,77]; i.e., the aqueous phase supersaturated by N_2. The EOS was first calibrated using experimental data for water-N_2 at 298.15, 308.15, 318.15, and 323.15 K from 80 to 1015 bara [78,79]. Then, it was calibrated for NaCl brine-N_2 using Smith et al. [70] and O'Sullivan and Smith [71], in which 1 M NaCl brine was used at 303.15, 324.65, 375.65, and 398.15 K from 12 to 608 bara. Although the experimental temperature in this research, 295.15 K, is not contained in the data of Smith et al. [70] and O'Sullivan and Smith [71,72], the N_2 solubility in NaCl brine at small molarities (e.g., 1 M) is insensitive to temperature. Also, the NaCl concentration in this research, 0.88 M, is close to the NaCl concentration, 1 M, for the data. Fig. 10 compares the calculated results using the GERG-2008 EOS with the experimental data in the literature for water-N_2 and NaCl brine-N_2. Results show good agreement between the EOS results and the data; therefore, the GERG-2008 EOS was successfully calibrated. Supplementary Material gives a detailed description of the GERG-2008 EOS model and parameters for the water-N_2 and NaCl brine-N_2 mixtures.

The experimental data given in Tables 2 and 3 were then used to solve the calibrated EOS for properties of aqueous NB dispersion of N_2 for the given temperature, total volume, mole numbers for water/brine and N_2, and external-phase pressure. Among these input variables, the

water mole numbers based on m_{w3} (Table 2) and m_{b3} (Table 3) were quite influential to the resulting diameter of bubbles. Tables 2 and 3 show that the uncertainty of m_{w3} (and m_{b3}) was ± 3 g. Even a minor variation (e.g., 0.1 g) in m_{w3} (or m_{b3}) significantly influenced the calculated apparent bubble diameter by one order of magnitude; therefore, it was not possible to quantitatively determine an apparent bubble diameter for these data with an order-of-magnitude accuracy using thermodynamic calculations only. Therefore, we allowed for adjustment in mole numbers of the two components within the uncertainty range such that the Helmholtz free energy was minimized while satisfying the specified temperature, total volume, and external pressure. We confirmed that such adjustments resulted in overall compositions within the uncertainty range stated above.

Figs. 11 and 12 show the results from the GERG-2008 EOS, such as bubble diameter, bubble number density, supersaturation of aqueous phase by N_2, the fraction of N_2 as bubble dispersion, and capillary pressure, for the N_2 NB fluid in DI water and NaCl brine, respectively. The error bars were determined as half the difference between the smallest and largest values at 104 bara (for DI water) since the experiment was repeated three times at this pressure. For the aqueous supersaturation levels (Fig. 11c and Fig. 12c), the N_2 concentration in the aqueous phase was compared with the inherent solubility of N_2 based on the GERG-2008 EOS. For Fig. 11d and Fig. 12d, the mole number of N_2 as bubbles was divided by the total mole number of N_2 for each sample.

Fig. 11ab and Fig. 12ab show that the calculated diameter decreased, and the number density of bubbles increased with increasing external pressure. For the DI water case, the extrapolation to atmospheric pressure using the two lowest pressure data yields a bubble diameter of 158 nm. This extrapolated diameter lies within the range of measured bubble diameters, 50–400 nm, at atmospheric pressure in the literature [1,21]. Also see Figs. 5, 7, and 9 for the data measured in this research. Fig. 11cd and 12 cd show that a large fraction of the N_2 in the system is molecularly dissolved in the external aqueous phase. That is, the existence of bubbles increases the N_2 content in the system by increasing the molecule dispersion (supersaturation) in the aqueous phase much more than by containing N_2 as bubbles. The presence of bubbles in aqueous NB fluid tends to increase the level of supersaturation in the external aqueous phase with capillary pressure (Fig. 11e and Fig. 12e). The results indicate that this supersaturation is the main contribution to the amount of N_2 in the aqueous NB fluid, which has fundamental impacts on the research and development of NB technologies.

Fig. 3 shows that the N_2 content did not substantially change between DI water and NaCl brine. However, comparison of Figs. 11 and 12 indicates that the NaCl salinity may have reduced the amount of N_2 that was molecularly dissolved, which required increasing the amount of N_2 as bubbles to satisfy the material balance in the closed system of the experiments in this research.

4. Conclusions

This paper presented a new set of experimental data for aqueous NB dispersions of N_2 at elevated pressures of up to 277 bara using N_2 and DI water or 0.88 M NaCl brine with specially designed stainless-steel porous membranes. The N_2 content in the generated NB sample was investigated for different parameters, such as pressure, salinity, co-injection ratio, total injection flow rate, and membrane pore diameter. The experimental results were supplemented with the GERG-2008 EOS model to give a qualitative overview of the characteristics of the aqueous NB fluid. The main conclusions are as follows:

1. The N_2 content in aqueous NB dispersion increased significantly with pressure. At 277 bara, for example, the inherent solubility of N_2 in DI water is 0.13 mol/L, but the N_2 content was enhanced to 0.29 mol/L by aqueous NB dispersion with DI water. With 0.88 M NaCl brine, the inherent solubility of N_2 is 0.11 mol/L at 274 bara, but the N_2 content was enhanced to 0.30 mol/L by aqueous NB dispersion. The impact of NaCl salinity on the N_2 content in aqueous NB dispersion was not observed for high-pressure experiments in this research.
2. The N_2 content in aqueous NB dispersion was insensitive to injection parameters, such as the total injection rate and the co-injection ratio, in this research. In particular, using a 2 μm membrane resulted in a similar gas content as using a 5 μm membrane.
3. Analysis of the experimental data using the GERG-2008 EOS showed that the apparent diameter of N_2 NBs ranged from 14 to 120 nm for DI water and 5 to 115 nm for 0.88 M NaCl brine under the experimental conditions. Additionally, the analysis indicated that NBs were not the main storage of N_2, but they enabled the supersaturation of the aqueous phase by N_2 enhancing the N_2 content in the system.
4. The DLS and NTA data measured for depressurized samples of aqueous NB dispersion of N_2 in this research showed transient behavior over 10 days. Number densities and size distributions of NBs were consistent with the reported data in the literature.

CRediT authorship contribution statement

Tesleem Lawal: Data curation, Formal analysis, Investigation, Methodology, Validation, Visualization, Writing – original draft. **Hao Wang:** Data curation, Formal analysis, Investigation, Methodology, Validation. **Ryosuke Okuno:** Conceptualization, Data curation, Formal analysis, Funding acquisition, Methodology, Project administration, Resources, Supervision, Validation, Writing – original draft, Writing – review & editing.

Declaration of competing interest

The authors declare that they have no known competing financial interests or personal relationships that could have appeared to influence the work reported in this paper.

Data availability

Data will be made available on request.

Acknowledgements

We gratefully acknowledge the members of the Energi Simulation Industrial Affiliate Program on Carbon Utilization and Storage (ES Carbon UT) at the Center for Subsurface Energy and the Environment at the University of Texas at Austin for their support. Ryosuke Okuno holds the Pioneer Corporation Faculty Fellowship in Petroleum Engineering at the University of Texas at Austin.

Appendix A. Supplementary data

Supplementary data to this article can be found online at https://doi.org/10.1016/j.molliq.2024.124340.

REFERENCES

[1] M. Alheshibri, J. Qian, M. Jehannin, V.S.J. Craig, A history of nanobubbles, Langmuir 32 (43) (2016) 11086–11100, https://doi.org/10.1021/acs.langmuir.6b02489.
[2] B.H. Tan, H. An, C.-D. Ohl, Stability of surface and bulk nanobubbles, Curr. Opin. Colloid Interface Sci. 53 (2021) 101428, https://doi.org/10.1016/j.cocis.2021.101428.
[3] T. Temesgen, T.T. Bui, M. Han, T. Kim, H. Park, Micro and nanobubble technologies as a new horizon for water-treatment techniques: A review, Adv. Colloid Interface Sci. 246 (2017) 40–51, https://doi.org/10.1016/j.cis.2017.06.011.
[4] J.N. Meegoda, S. Aluthgun Hewage, J.H. Batagoda, Stability of nanobubbles, Environ. Eng. Sci. 35 (11) (2018) 1216–1227, https://doi.org/10.1089/ees.2018.0203.
[5] A.J. Jadhav, M. Barigou, Bulk nanobubbles or not nanobubbles: That is the question, Langmuir 36 (7) (2020) 1699–1708, https://doi.org/10.1021/acs.langmuir.9b03532.

[6] K. Ebina, K. Shi, M. Hirao, J. Hashimoto, Y. Kawato, S. Kaneshiro, T. Morimoto, K. Koizumi, H. Yoshikawa, Oxygen and air nanobubble water solution promote the growth of plants, fishes, and mice, PLoS One 8 (6) (2013) e65339.
[7] S.H. Oh, J.G. Han, J.-M. Kim, Long-term stability of hydrogen nanobubble fuel, Fuel 158 (2015) 399–404, https://doi.org/10.1016/j.fuel.2015.05.072.
[8] Y.A. Perez Sirkin, E.D. Gadea, D.A. Scherlis, V. Molinero, Mechanisms of nucleation and stationary states of electrochemically generated nanobubbles, J. Am. Chem. Soc. 141 (27) (2019) 10801–10811, https://doi.org/10.1021/jacs.9b04479.
[9] D.V.B. Batchelor, F.J. Armistead, N. Ingram, S.A. Peyman, J.R. Mclaughlan, P. L. Coletta, S.D. Evans, Nanobubbles for therapeutic delivery: production, stability and current prospects, Curr. Opin. Colloid Interface Sci. 54 (2021) 101456, https://doi.org/10.1016/j.cocis.2021.101456.
[10] E.P. Favvas, G.Z. Kyzas, E.K. Efthimiadou, A.C. Mitropoulos, Bulk nanobubbles, generation methods and potential applications, Curr. Opin. Colloid Interface Sci. 54 (2021) 101455, https://doi.org/10.1016/j.cocis.2021.101455.
[11] P. Pal, A. Joshi, H. Anantharaman, Nanobubble ozonation for waterbody rejuvenation at different locations in India: A holistic and sustainable approach, Results Eng. 16 (2022) 100725, https://doi.org/10.1016/j.rineng.2022.100725.
[12] M.A. Oturan, J.-J. Aaron, Advanced oxidation processes in water/wastewater treatment: principles and applications. A review, Crit. Rev. Environ. Sci. Technol. 44 (23) (2014) 2577–2641, https://doi.org/10.1080/10643389.2013.829765.
[13] A.J. Atkinson, O.G. Apul, O. Schneider, S. Garcia-Segura, P. Westerhoff, Nanobubble technologies offer opportunities to improve water treatment, Acc. Chem. Res. 52 (5) (2019) 1196–1205, https://doi.org/10.1021/acs.accounts.8b00606.
[14] T. Lyu, S. Wu, R.J.G. Mortimer, G. Pan, Nanobubble technology in environmental engineering: Revolutionization potential and challenges, Environ. Sci. Technol. 53 (13) (2019) 7175–7176, https://doi.org/10.1021/acs.est.9b02821.
[15] I. Levitsky, D. Tavor, V. Gitis, Micro and nanobubbles in water and wastewater treatment: A state-of-the-art review, J. Water Process Eng. 47 (2022) 102688, https://doi.org/10.1016/j.jwpe.2022.102688.
[16] M. Jia, M.U. Farid, J.A. Kharraz, N.M. Kumar, S.S. Chopra, A. Jang, J. Chew, S. K. Khanal, G. Chen, A.K. An, Nanobubbles in water and wastewater treatment systems: Small bubbles making big difference, Water Res. 245 (2023) 120613, https://doi.org/10.1016/j.watres.2023.120613.
[17] G. Liu, Z. Wu, V.S.J. Craig, Cleaning of protein-coated surfaces using nanobubbles: An investigation using a quartz crystal microbalance, J. Phys. Chem. C 112 (43) (2008) 16748–16753, https://doi.org/10.1021/jp805143c.
[18] G. Liu, V.S.J. Craig, Improved cleaning of hydrophilic protein-coated surfaces using the combination of nanobubbles and SDS, ACS Appl. Mater. Interfaces 1 (2) (2009) 481–487, https://doi.org/10.1021/am800150p.
[19] M. Zhang, J.R.T. Seddon, Nanobubble-nanoparticle interactions in bulk solutions, Langmuir 32 (43) (2016) 11280–11286, https://doi.org/10.1021/acs.langmuir.6b02419.
[20] J. Zhu, H. An, M. Alheshibri, L. Liu, P.M.J. Terpstra, G. Liu, V.S.J. Craig, Cleaning with bulk nanobubbles, Langmuir 32 (43) (2016) 11203–11211, https://doi.org/10.1021/acs.langmuir.6b01004.
[21] L. Zhou, S. Wang, L. Zhang, J. Hu, Generation and stability of bulk nanobubbles: A review and perspective, Curr. Opin. Colloid Interface Sci. 53 (2021) 101439, https://doi.org/10.1016/j.cocis.2021.101439.
[22] G. Han, S. Chen, S. Su, Y. Huang, B. Liu, H. Sun, A review and perspective on micro and nanobubbles: What they are and why they matter, Miner. Eng. 189 (2022) 107906, https://doi.org/10.1016/j.mineng.2022.107906.
[23] A.W. Foudas, R.I. Kosheleva, E.P. Favvas, M. Kostoglou, A.C. Mitropoulos, G. Z. Kyzas, Fundamentals and applications of nanobubbles: A review, Chem. Eng. Res. Des. 189 (2023) 64–86, https://doi.org/10.1016/j.cherd.2022.11.013.
[24] X. Li, B. Peng, Q. Liu, J. Liu, L. Shang, Micro and nanobubbles technologies as a new horizon for CO_2-EOR and CO_2 geological storage techniques: A review, Fuel 341 (2023) 127661, https://doi.org/10.1016/j.fuel.2023.127661.
[25] K. Ohgaki, N.Q. Khanh, Y. Joden, A. Tsuji, T. Nakagawa, Physicochemical approach to nanobubble solutions, Chem. Eng. Sci. 65 (3) (2010) 1296–1300, https://doi.org/10.1016/j.ces.2009.10.003.
[26] N. Nirmalkar, A.W. Pacek, M. Barigou, On the existence and stability of bulk nanobubbles, Langmuir 34 (37) (2018) 10964–10973, https://doi.org/10.1021/acs.langmuir.8b01163.
[27] H. Oliveira, A. Azevedo, J. Rubio, Nanobubbles generation in a high-rate hydrodynamic cavitation tube, Miner. Eng. 116 (2018) 32–34, https://doi.org/10.1016/j.mineng.2017.10.020.
[28] K. Kikuchi, Y. Tanaka, Y. Saihara, M. Maeda, M. Kawamura, Z. Ogumi, Concentration of hydrogen nanobubbles in electrolyzed water, J. Colloid Interface Sci. 298 (2) (2006) 914–919, https://doi.org/10.1016/j.jcis.2006.01.010.
[29] K. Kikuchi, S. Nagata, Y. Tanaka, Y. Saihara, Z. Ogumi, Characteristics of hydrogen nanobubbles in solutions obtained with water electrolysis, J. Electroanal. Chem. 600 (2) (2007) 303–310, https://doi.org/10.1016/j.jelechem.2006.10.005.
[30] K. Kikuchi, A. Ioka, T. Oku, Y. Tanaka, Y. Saihara, Z. Ogumi, Concentration determination of oxygen nanobubbles in electrolyzed water, J. Colloid Interface Sci. 329 (2) (2009) 306–309, https://doi.org/10.1016/j.jcis.2008.10.009.
[31] Z. Fang, L. Wang, X. Wang, L. Zhou, S. Wang, Z. Zou, R. Tai, L. Zhang, J. Hu, Formation and stability of surface/bulk nanobubbles produced by decompression at lower gas concentration, J. Phys. Chem. C 122 (39) (2018) 22418–22423, https://doi.org/10.1021/acs.jpcc.8b05688.
[32] S. Ke, W. Xiao, N. Quan, Y. Dong, L. Zhang, J. Hu, Formation and stability of bulk nanobubbles in different solutions, Langmuir 35 (15) (2019) 5250–5256, https://doi.org/10.1021/acs.langmuir.9b00144.
[33] W. Xu, Y. Wang, Q. Huang, X. Wang, L. Zhou, X. Wang, B. Wen, N. Guan, J. Hu, X. Zhou, L. Zhang, The generation and stability of bulk nanobubbles by compression-decompression method: the role of dissolved gas, Colloids Surf. A Physicochem. Eng. Asp. 657 (2023) 130488, https://doi.org/10.1016/j.colsurfa.2022.130488.
[34] M. Kukizaki, M. Goto, Size control of nanobubbles generated from shirasu-porous-glass (SPG) membranes, J. Membr. Sci. 281 (1–2) (2006) 386–396, https://doi.org/10.1016/j.memsci.2006.04.007.
[35] A.K.A. Ahmed, C. Sun, L. Hua, Z. Zhang, Y. Zhang, W. Zhang, T. Marhaba, Generation of nanobubbles by ceramic membrane filters: The dependence of bubble size and zeta potential on surface coating, pore size and injected gas pressure, Chemosphere 203 (2018) 327–335, https://doi.org/10.1016/j.chemosphere.2018.03.157.
[36] K. Ulatowski, P. Sobieszuk, A. Mróz, T. Ciach, Stability of nanobubbles generated in water using porous membrane system, Chem. Eng. Process. - Process Intesif. 136 (2019) 62–71, https://doi.org/10.1016/j.cep.2018.12.010.
[37] J. Jin, Z. Feng, F. Yang, N. Gu, Bulk nanobubbles fabricated by repeated compression of microbubbles, Langmuir 35 (12) (2019) 4238–4245, https://doi.org/10.1021/acs.langmuir.8b04314.
[38] J. Jin, R. Wang, J. Tang, L. Yang, Z. Feng, C. Xu, F. Yang, N. Gu, Dynamic tracking of bulk nanobubbles from microbubbles shrinkage to collapse, Colloids Surf A Physicochem Eng Asp 589 (2020) 124430, https://doi.org/10.1016/j.colsurfa.2020.124430.
[39] S.H. Oh, J.-M. Kim, Generation and stability of bulk nanobubbles, Langmuir 33 (15) (2017) 3818–3823, https://doi.org/10.1021/acs.langmuir.7b00510.
[40] P.S. Epstein, M.S. Plesset. On the Stability of Gas Bubbles in Liquid-Gas Solutions. 1950.
[41] Q. Wang, H. Zhao, N. Qi, Y. Qin, X. Zhang, Y. Li, Generation and stability of size-adjustable bulk nanobubbles based on periodic pressure change, Sci. Rep. 9 (1) (2019) 1118, https://doi.org/10.1038/s41598-018-38066-5.
[42] S.A. Hewage, J. Kewalramani, J.N. Meegoda, Stability of nanobubbles in different salts solutions, Colloids Surf. A Physicochem. Eng. Asp. 609 (2021) 125669, https://doi.org/10.1016/j.colsurfa.2020.125669.
[43] F.Y. Ushikubo, T. Furukawa, R. Nakagawa, M. Enari, Y. Makino, Y. Kawagoe, T. Shiina, S. Oshita, Evidence of the existence and the stability of Nano-bubbles in water, Colloids Surf. A Physicochem. Eng. Asp. 361 (1–3) (2010) 31–37, https://doi.org/10.1016/j.colsurfa.2010.03.005.
[44] A. Azevedo, R. Etchepare, S. Calgaroto, J. Rubio, Aqueous dispersions of nanobubbles: generation, properties and features, Min Eng. 94 (2016) 29–37, https://doi.org/10.1016/j.mineng.2016.05.001.
[45] H.S. Alam, P. Sutikno, T.A.F. Soelaiman, A.T. Sugiarto, Bulk nanobubbles: Generation using a two-chamber swirling flow nozzle and long-term stability in water, J Flow Chem. 12 (2) (2022) 161–173, https://doi.org/10.1007/s41981-021-00208-8.
[46] M. Alheshibri, V.S.J. Craig, Armoured nanobubbles; ultrasound contrast agents under pressure, J. Colloid Interface Sci. 537 (2019) 123–131, https://doi.org/10.1016/j.jcis.2018.10.108.
[47] M. Alheshibri, M. Jehannin, V.A. Coleman, V.S.J. Craig, Does gas supersaturation by a chemical reaction produce bulk nanobubbles? J. Colloid Interface Sci. 554 (2019) 388–395, https://doi.org/10.1016/j.jcis.2019.07.016.
[48] T. Uchida, S. Oshita, M. Ohmori, T. Tsuno, K. Soejima, S. Shinozaki, Y. Take, K. Mitsuda, Transmission electron microscopic observations of nanobubbles and their capture of impurities in wastewater, Nanoscale Res. Lett. 6 (1) (2011) 295, https://doi.org/10.1186/1556-276X-6-295.
[49] J. Rabinowitz, E. Whittier, Z. Liu, K. Jayant, J. Frank, K. Shepard, Nanobubble-controlled nanofluidic transport, Sci. Adv. 6 (46) (2020) eabd0126, https://doi.org/10.1126/sciadv.abd0126.
[50] R. Christensen. Carbonated Waterflood Results–Texas And Oklahoma. Annual Meeting of Rocky Mountain Petroleum Engineers of AIME, Farmington, New Mexico, USA, 1961; SPE-66-MS. https://doi.org/10.2118/66-MS.
[51] T.A. Blackford. Carbonated Waterflood Implementation and Its Impact on Material Performance in a Pilot Project. SPE Annual Technical Conference and Exhibition, Dallas, Texas, 1987; SPE-16831-MS. https://doi.org/10.2118/16831-MS.
[52] J.M. Perez. Carbonated Water Imbibition Flooding: An Enhanced Oil Recovery Process for Fractured Reservoirs. 1992, 12.
[53] Y. Dong, B. Dindoruk, C. Ishizawa, E. Lewis, T. Kubicek. An Experimental Investigation of Carbonated Water Flooding. SPE Annual Technical Conference and Exhibition, Denver, Colorado, USA, 2011; SPE-145380-MS. https://doi.org/10.2118/145380-MS.
[54] M. Riazi, M. Sohrabi, M. Jamiolahmady, Experimental study of pore-scale mechanisms of carbonated water injection, Transp. Porous Med. 86 (1) (2011) 73–86, https://doi.org/10.1007/s11242-010-9606-8.
[55] M. Sohrabi, N.I. Kechut, M. Riazi, M. Jamiolahmady, S. Ireland, G. Robertson, Safe storage of CO_2 together with improved oil recovery by CO_2-enriched water injection, Chem. Eng. Res. Des. 89 (9) (2011) 1865–1872, https://doi.org/10.1016/j.cherd.2011.01.027.
[56] M. Sohrabi, A. Emadi, S.A. Farzaneh, S. Ireland. A Thorough Investigation of Mechanisms of Enhanced Oil Recovery by Carbonated Water Injection. SPE Annual Technical Conference and Exhibition, Houston, Texas, USA, 2015; SPE-175159-MS. https://doi.org/10.2118/175159-MS.
[57] J. Foroozesh, M. Jamiolahmady, M. Sohrabi, Mathematical modeling of carbonated water injection for EOR and CO_2 storage with a focus on mass transfer kinetics, Fuel 174 (2016) 325–332, https://doi.org/10.1016/j.fuel.2016.02.009.
[58] M. Seyyedi, P. Mahzari, M. Sohrabi, A comparative study of oil compositional variations during CO_2 and carbonated water injection scenarios for EOR, J. Pet. Sci. Eng. 164 (2018) 685–695, https://doi.org/10.1016/j.petrol.2018.01.029.

[59] C. Esene, N. Rezaei, A. Aborig, S. Zendehboudi, Comprehensive review of carbonated water injection for enhanced oil recovery, Fuel 237 (2019) 1086–1107, https://doi.org/10.1016/j.fuel.2018.08.106.
[60] G. Bisweswar, A. Al-Hamairi, S. Jin, Carbonated water injection: an efficient EOR approach. A review of fundamentals and prospects, J. Petrol. Explor. Prod. Technol. 10 (2) (2020) 673–685, https://doi.org/10.1007/s13202-019-0738-2.
[61] E. Ajoma, T. Sungkachart, Saira, H. Yin, F. Le-Hussain, A laboratory study of coinjection of water and CO_2 to improve oil recovery and CO_2 storage: Effect of fraction of CO_2 injected, SPE J. 26 (04) (2021) 2139–2147, https://doi.org/10.2118/204464-PA.
[62] A. Talebi, A. Hasan-Zadeh, Y. Kazemzadeh, M. Riazi, A review on the application of carbonated water injection for EOR purposes: Opportunities and challenges, J. Pet. Sci. Eng. 214 (2022) 110481, https://doi.org/10.1016/j.petrol.2022.110481.
[63] D. Liu, R. Agarwal, Y. Li, S. Yang, Reactive transport modeling of mineral carbonation in unaltered and altered basalts during CO_2 sequestration, Int. J. Greenhouse Gas Control 85 (2019) 109–120, https://doi.org/10.1016/j.ijggc.2019.04.006.
[64] S.Ó. Snæbjörnsdóttir, B. Sigfússon, C. Marieni, D. Goldberg, S.R. Gislason, E. H. Oelkers, Carbon dioxide storage through mineral carbonation, Nat. Rev. Earth Environ. 1 (2) (2020) 90–102, https://doi.org/10.1038/s43017-019-0011-8.
[65] C. Marieni, M. Voigt, D.E. Clark, S.R. Gíslason, E.H. Oelkers, Mineralization potential of water-dissolved CO_2 and H_2S injected into basalts as function of temperature: freshwater versus seawater, Int. J. Greenhouse Gas Control 109 (2021) 103357, https://doi.org/10.1016/j.ijggc.2021.103357.
[66] A. Raza, G. Glatz, R. Gholami, M. Mahmoud, S. Alafnan, Carbon mineralization and geological storage of CO_2 in basalt: Mechanisms and technical challenges, Earth Sci. Rev. 229 (2022) 104036, https://doi.org/10.1016/j.earscirev.2022.104036.
[67] H. Wang, O. Carrasco-Jaim, R. Okuno. Aqueous Nanobubble Dispersion of CO_2 in Sodium Formate Solution for Enhanced CO_2 Mineralization Using Basaltic Rocks, the 2024 Carbon Capture, Utilization, and Storage conference, March 11 - 13, 2024, Houston, Texas.
[68] R. Wiebe, V.L. Gaddy, C. Heins, Solubility of nitrogen in water at 25°C from 25 to 1000 atmospheres, Ind. Eng. Chem. 24 (8) (1932) 927, https://doi.org/10.1021/ie50272a023.
[69] D. L. Parkhurst , C. A. J. Appelo , Description of Input and Examples for PHREEQC Version 3–A Computer Program for Speciation, Batch-Reaction, One-Dimensional Transport, and Inverse Geochemical Calculations , U.S. Geological Survey Techniques and Methods, United States Geological Survey (USGS . https://pubs.usgs.gov/tm/06/a43/).
[70] N.O. Smith, S. Kelemen, B. Nagy, Solubility of natural gases in aqueous salt solutions—II, Geochim. Cosmochim. Acta 26 (9) (1962) 921–926, https://doi.org/10.1016/0016-7037(62)90066-2.
[71] T.D. O'Sullivan, N.O. Smith, Solubility and partial molar volume of nitrogen and methane in water and in aqueous sodium chloride from 50 to 125.Deg. and 100 to 600 atm, J. Phys. Chem. 74 (7) (1970) 1460–1466, https://doi.org/10.1021/j100702a012.
[72] T.D. O'Sullivan, N.O. Smith, B. Nagy, Solubility of natural gases in aqueous salt solutions—III nitrogen in aqueous NaCl at high pressures, Geochim. Cosmochim. Acta 30 (6) (1966) 617–619, https://doi.org/10.1016/0016-7037(66)90015-9.
[73] S.H. Achour, R. Okuno, Phase stability analysis for tight porous media by minimization of the helmholtz free energy, Fluid Phase Equilib. 520 (2020) 112648, https://doi.org/10.1016/j.fluid.2020.112648.
[74] S.H. Achour, K. Sheng, T. Lawal, R. Okuno. Thermodynamic Modeling of Aqueous Nanobubble Dispersion. SPE Annual Technical Conference and Exhibition, San Antonio, Texas, USA, 2023. https://doi.org/10.2118/215122-MS.
[75] O. Kunz, W. Wagner, The GERG-2008 wide-range equation of state for natural gases and other mixtures: An expansion of GERG-2004, J. Chem. Eng. Data 57 (11) (2012) 3032–3091, https://doi.org/10.1021/je300655b.
[76] A.R. Imre, A. Baranyai, U.K. Deiters, P.T. Kiss, T. Kraska, S.E. Quiñones Cisneros, Estimation of the thermodynamic limit of overheating for bulk water from interfacial properties, Int. J. Thermophys. 34 (11) (2013) 2053–2064, https://doi.org/10.1007/s10765-013-1518-8.
[77] P. Aursand, M.A. Gjennestad, E. Aursand, M. Hammer, Ø. Wilhelmsen, The spinodal of single- and multi-component fluids and its role in the development of modern equations of state, Fluid Phase Equilib. 436 (2017) 98–112, https://doi.org/10.1016/j.fluid.2016.12.018.
[78] V.Y. Maslennikova, Solubility of nitrogen in water, Tr. Gos. Nauchno-Issled. Proektn. Inst. Azotn. Prom-Sti. Prod. Org. Sint. 12 (1971) 82–87.
[79] Y. Liu, M. Hou, H. Ning, D. Yang, G. Yang, B. Han, Phase equilibria of $CO_2 + N_2 + H_2O$ and $N_2 + CO_2 + H_2O + NaCl + KCl + CaCl_2$ systems at different temperatures and pressures, J. Chem. Eng. Data 57 (7) (2012) 1928–1932, https://doi.org/10.1021/je3000958.